Dynamical Torque in $Co_xFe_{3−x}O_4$ Nanocube Thin Films Characterized by Femtosecond Magneto-Optics: A π-Shift Control of the Magnetization Precession

Mircea Vomir,*,[†] Robin Turnbull,[‡] Ipek Birced,[‡] Pedro Parreira,[§] Donald A. MacLaren,[§] Stephen L. Lee,[‡] Pascal André,*,[‡,∥,⊥] and Jean-Yves Bigot*,[†]

[†]Institut de Physique et Chimie des Matériaux de Strasbourg, UMR 7504, CNRS, Université de Strasbourg, BP 43, 23 rue du Loess, 67034 Strasbourg Cedex 02, France

[‡]SUPA, School of Physics and Astronomy, University of St. Andrews, St Andrews KY16 9SS, United Kingdom

[§]SUPA, Department of Physics and Astronomy, University of Glasgow, Glasgow G12 8QQ, United Kingdom

[∥]Elements Chemistry Laboratory, RIKEN, Wako 351-0198, Japan

[⊥]Department of Physics, CNRS-Ewha International Research Center, Ewha W. University, Seoul 120-750, Republic of Korea

Ⓢ Supporting Information

ABSTRACT: For spintronic devices excited by a sudden magnetic or optical perturbation, the torque acting on the magnetization plays a key role in its precession and damping. However, the torque itself can be a dynamical quantity via the time-dependent anisotropies of the system. A challenging problem for applications is then to disentangle the relative importance of various sources of anisotropies in the dynamical torque, such as the dipolar field, the crystal structure or the shape of the particular interacting magnetic nanostructures. Here, we take advantage of a range of colloidal cobalt ferrite nanocubes assembled in 2D thin films under controlled magnetic fields to demonstrate that the phase, ϕ_{Prec}, of the precession carries a strong signature of the dynamical anisotropies. Performing femtosecond magneto-optics, we show that ϕ_{Prec} displays a π-shift for a particular angle θ_H of an external static magnetic field, **H**. θ_H is controlled with the cobalt concentration, the laser intensity, as well as the interparticle interactions. Importantly, it is shown that the shape anisotropy, which strongly departs from those of equivalent bulk thin films or individual noninteracting nanoparticles, reveals the essential role played by the interparticle collective effects. This work shows the reliability of a noninvasive optical approach to characterize the dynamical torque in high density magnetic recording media made of organized and interacting nanoparticles.

KEYWORDS: Magnetization dynamics, magnetic torque, colloidal magnetic nanoparticles, ferrite nanocubes, 2D nanoparticle films, ultrafast magneto-optics

D esigning complex nanostructures with controlled magnetic anisotropy is of utmost importance for innovative information processing technologies like spin-torque oscillators,[1,2] as well as for medical applications such as cancer therapy.[3−5] For instance, the current data storage devices use highly anisotropic ferromagnetic nanostructures that provide large densities of information. Simultaneously, a faster manipulation of the magnetization is receiving lots of attention. In that context, emerging technologies aim at combining high temporal and spatial resolutions for the study of structures with reduced dimensionality.[6] This can be achieved using femtosecond laser pulses to study and control the magnetization in a variety of nanosystems.[7−19] Among the possible colloidal magnetic nanoparticle model systems,[20−23] iron oxide nanoparticles are attractive due to the possibility to readily tailor their composition, obtain well-defined shapes, and form superstructures.[24−28] In addition, their magneto-crystalline

anisotropy can be tuned by metal doping with cobalt ions for example.[29−31]

Here, considering the potentials associated with nanoparticle collective effects, we investigate ultrafast magnetization dynamics in concentrated nanoparticles assembled in two-dimensional (2D) thin films. We use the cobalt content to tune the anisotropy of ferrite nanocubes ($Co_xFe_{3−x}O_4$), and we explore the effect of interparticle interactions by magnetically "stamping" with an external field the films during their formation. We then evidence for the first time that the precession dynamics of the magnetization in single layer cobalt ferrite nanocubes is controlled by the interplay between the time dependent magneto-crystalline and shape anisotropies. We show that the precession can oscillate with opposite phase
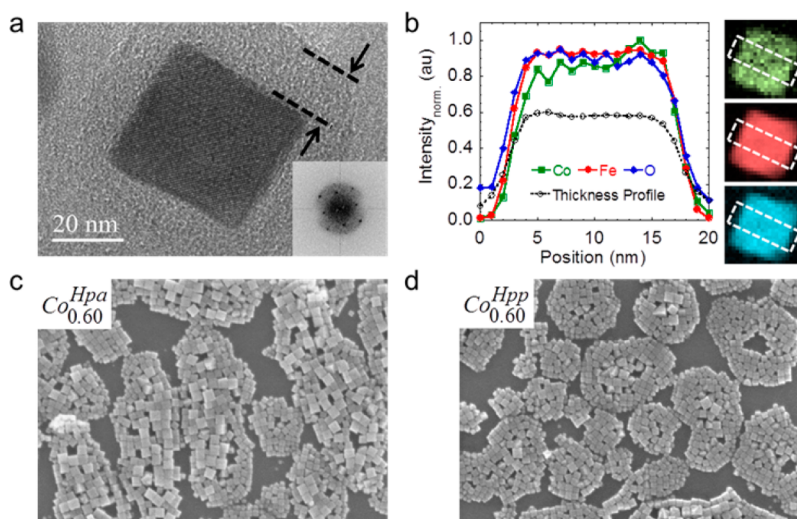
Figure 1. Structural and morphological characterizations of $Co_xFe_{3-x}O_4$ nC thin films. (a) High-magnification transmission electron microscopy (TEM) image of a single crystal undoped nanoparticle; the arrows illustrate a carbonaceous, lower density material surrounding the nCs. Inset: Fourier transform a square region that comprises the nanoparticle only. (b) Normalized elemental distribution given by electron energy loss spectroscopy (EELS) on a single 33% Co-doped nanocube with, from top to bottom, cobalt, iron, and oxygen elemental maps obtained from the same spectrum image. (c,d) SEM images of $Co_{0.6}^{Hpa}$ and $Co_{0.6}^{Hpp}$, respectively.
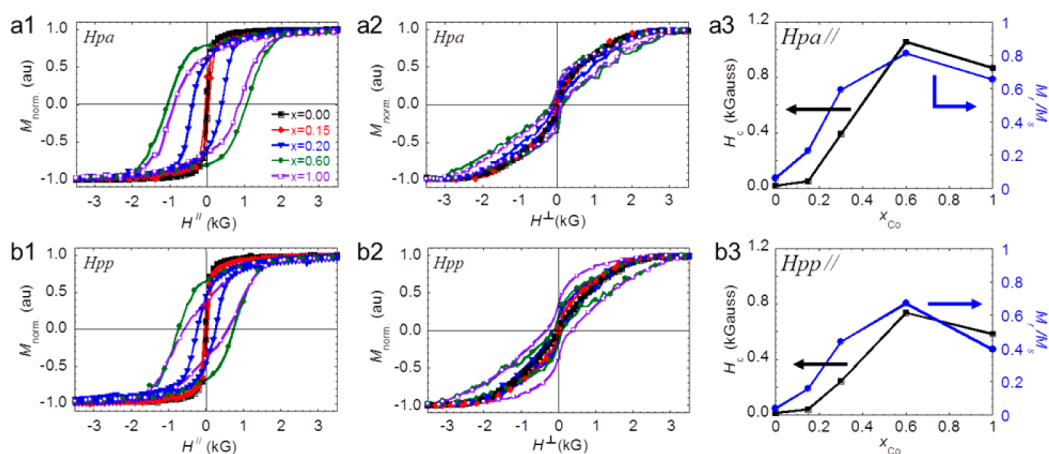

Figure 2. Magnetic characterization obtained at room temperature of ferrite $Co_xFe_{3-x}O_4$ nC thin films prepared with a parallel (Hpa) (a) and perpendicular (Hpp) (b) magnetic field. The SQUID magnetic field was parallel (//) (1) and perpendicular ($\perp$) (2) to the surface of the nC films, coercivity (black square) and remnant to saturation magnetization ratio (blue circle) of the nCs (3). Cobalt content $x = 0.00$ (0%, black square), 0.15 (5%, red diamond), 0.30 (10%, blue inverted triangle), 0.60 (20%, green circle), 1.00 (33%, purple open square).

when varying the angle of an external magnetic field θ_H. This phase opposition occurs abruptly for a particular angle $\overline{\theta_H}$. which depends on the concentration of Co, the laser intensity, and the degree of organization of the nanocubes.

A range of colloidal iron oxide nanocubes (nCs) with controlled cobalt doping were prepared by solution chemistry under inert nitrogen atmosphere according to a protocol detailed in the SI and based on the literature.[28,32−35] Noticing that while the use of the external magnetic field has been explored to drive nanoparticles organization[28,36−38] the effect of its orientation relative to the organization interface on the dynamics of interparticle interactions has received no attention, the nCs were deposited at a water/air interface and transferred onto quartz substrates with and without applying a magnetic field. Hereafter, the different samples are identified as Co_x^y. The cobalt concentration x was varied from 0 to one-third of the metal molar content with the values of $x = 0$, 0.15, 0.30, 0.60, and 1.00. During the formation of the films, a 4 kOe static

magnetic field was applied parallel (y = Hpa) or perpendicular (y = Hpp) to the substrate plane, while y = H0 corresponds to the film preparation without field.

Figure 1a displays a typical transmission electron microscopy (TEM) image of a single nC. Noticeably, the cubes tend to present a diffuse "shell" with a thickness of a few nanometers. This low electron density encapsulation is consistent with amorphous carbonaceous material remaining from the synthesis and not fully removed during the purification. The X-ray diffraction data (Figure S2a) demonstrate the crystallinity of the nanocubes and the lattice parameter is shown to slightly increase with the Co content (Figure S2b). The surface of the nanocubes is also highly crystalline (Figure 1a and Figure S3b,e,h). This is further illustrated by the TEM images and selected area electron diffraction (SAED) patterns obtained with the nanocubes (inset Figure 1a and Figure S3c,f,i). Overall, high-resolution electron microscope images and elemental analysis, as measured by electron energy loss spectroscopy
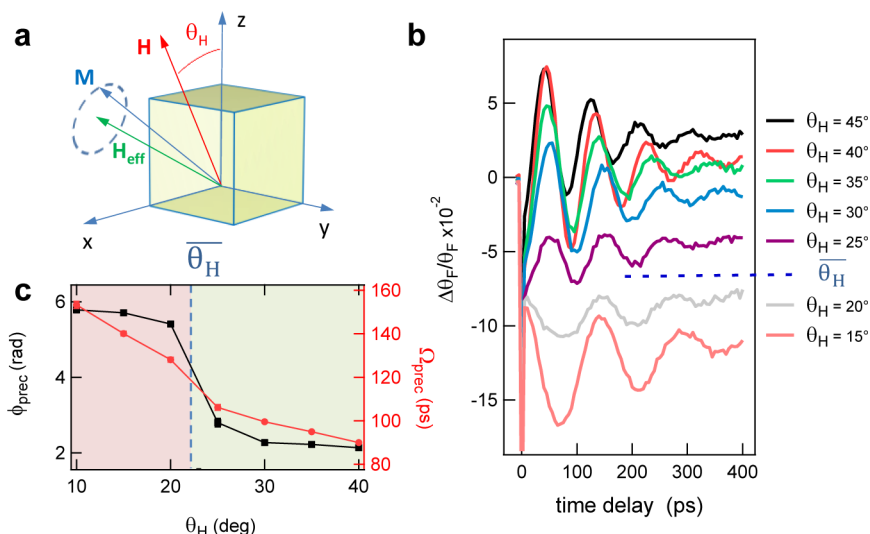
Figure 3. Ultrafast magnetization dynamics of $Co_xFe_{3-x}O_4$ nC single layers. (a) Schematic representation in a Cartesian co-ordinate system of the nanocubes in the xOy plane, showing the effective magnetic field $\mathbf{H}_{eff}$, the applied static magnetic field $\mathbf{H}_0$ and its orientation angle θ_H. (b) Typical time-resolved magneto-optical results, obtained in the Faraday geometry for several angles θ_H. (c) Variation of the precession period (Ω_{Prec}, red circle) and phase (ϕ_{Prec}, black square) as a function of the magnetic field orientation (θ_H). The sample $Co_{0.3}^{Hpa}$ was used for (b,c).

(EELS), showed that neither the iron distribution nor the Co-doping result in core−shell structures and demonstrated the formation of single crystal nCs (Figure 1a,b, and Figures S3−S5).

The 2D films transferred onto silicon substrates were investigated by scanning electron microscopy (SEM), which at low magnification showed a homogeneous distribution of the material across the substrates. At higher magnification, the films revealed more anisotropic magnetic nanoparticle islands in which morphology was influenced by the orientation of the external magnetic field applied during the organization process. As a result, quasi single layer islands grown with a parallel field were more acicular and cigar-shaped (Figure 1c), while with a perpendicular field, the islands tended to show a more circular shape (Figure 1c). These structures are consistent with magnetic particle organizations on solid substrates obtained under controlled solvent evaporation rate and magnetic fields.[38−40] These morphologies were observed with different sizes of domains and shapes of the islands for each dopant concentration (Figures S6, S7, and S8).

Figure 2a,b presents the static magnetization curves for the Co_x^{Hpa} and Co_x^{Hpp} samples, respectively, and illustrates the impact of orienting the magnetic field parallel and perpendicular to the nC film during its formation. Two important features are observed. The first is related to the measurement configuration. Measurements completed in the in-plane configuration (Figure 2a1,b1) present a the larger coercivity compared to those obtained in the perpendicular configuration (Figure 2a2,b2). The wider and more square hysteresis curves show that the sample magnetization tends to align in the plane of the nanoparticle film due to dipolar interactions between the nanocubes.[41−] This was observed for all the samples. The second important feature relates to the orientation of the external magnetic field used to prepare the nanoparticle thin films. The amplitude of H_c is larger and the hysteresis curves are again more square for the films formed under a parallel magnetic field (Figure 2a) than when the field was perpendicular (Figure 2b) to the film during its growth. This is due to a greater degree of particles organization in the parallel

field growth case, which is also shown in the SEM analysis (Figures S6−S8), and is consistent with the distribution of the anisotropy axes leading to a decrease of the squareness of the hysteresis curves. The coercive fields and remnant magnetization values are summarized in Table S2. The coercivity, as well as the ratio M_r/M_s, increases with the doping and shows a maximum for $x = 0.6$ (Co 20%, Figure 2a3,b3). The overall behavior is consistent with previous studies showing high coercivities for intermediate Co concentrations around 20%.[30] The decrease of the coercivity at higher concentrations is attributed to a displacement of the Co ions from octahedral to tetrahedral sites of the spinel structure, which results in a decrease of the anisotropy.

Although a few studies have considered the ultrafast magnetization dynamics of ferrite and cobalt ferrite spherical nanoparticles,[46−49] they were performed on dilute samples to avoid dipolar interactions and therefore were limited to studying the effects of size and coating of the nanoparticles. Laser-induced magnetization precession has not yet been explored in such systems. In this study, addressing the potentials arising from collective effects in concentrated samples, we investigate the ultrafast magnetization dynamics in nanoparticle thin films, which we magnetically "stamp" during the layer deposition and in which the cobalt content, hence the anisotropy, has been varied.

We performed the time-resolved magneto-optical experiments in the Faraday geometry using an amplified Ti:sapphire laser system with a repetition rate of 5 kHz. The pump and probe pulses had a duration of 120 and 150 fs, respectively. The probe beam had the fundamental wavelength of the amplifier (800 nm) while the pump was frequency doubled to 400 nm. They were both focused on the sample within a spot size of 50 and 100 μm, respectively, with an angle of incidence of 5°. The pump incident density of energy, E_{pump}, was set in the range of 1−10 mJ·cm^{-2}. For each film, we measured simultaneously (i) the static transmission T, (ii) the Faraday rotation θ_F, as well as their corresponding dynamical differential quantities $\Delta T(t)/T$, and $\Delta\theta_F(t)/\theta_F$, as a function of the pump probe delay, t.

As illustrated in Figure 3a, the sample was in the xOy plane, while the pump and probe pulses were along the Oz direction. A static magnetic field, $|H_0| \leq 3.5$ kOe, was rotated in the xOz plane. The Faraday rotation, θ_F, was obtained from the difference between two complementary angles of the magnetic field (θ_H, and $\pi - \theta_H$).

The absorption of the laser pulses by the nCs leads to an initial rise of the electrons and spins temperatures, which subsequently equilibrate with the lattice in a picosecond time scale.[7] This temperature rise modifies the effective magnetic field leading to a precession of the magnetization which was measured for several angles, θ_H, as shown in Figure 3b for the sample $Co_{0.3}^{Hpa}$. For each angle θ_H, the corresponding phase and period of the precession were obtained and are displayed in Figure 3c. It shows two important features. First, an abrupt change of the precession phase, ϕ_{Prec}, occurs around $\theta_H \approx 25°$. As demonstrated later, it results from the competition between the temperature dependent cubic magneto-crystalline anisotropy of the individual nanoparticles and the time-dependent demagnetizing field modified by the change of the magnetization modulus, which in the present case is a signature of the interaction between the nanocubes. Second, the precession period, Ω_{Prec}, continuously increases as θ_H decreases. It is also due to dipolar interactions between the nanoparticles.

Figure 4 presents the detailed analysis of the impact on the magnetization precession of the magneto-crystalline anisotropy controlled with Co-doping (Figure 4a), the degree of organization of the nCs (Figure 4b), as well as the density of energy of the pump laser E_{pump} (Figure 4c). In Figure 4a, $Co_{0.3}^{Hpa}$ and $Co_{0.6}^{Hpa}$ display an abrupt change of the precession phase around $\overline{\theta}_H = 25°$ for a pump density of excitation $E_{pump} = 3.6$ mJ cm^{-2}. At low cobalt concentration ($x \leq 0.15$), the small amplitude of the precession signal does not allow reliable extraction of phase and frequency for $\theta_H \leq 20°$. It should be emphasized that this situation occurs for low Co doping due to the lower anisotropy of the nCs as seen in Figure 2a3,b3. However, if a change of the precession phase is present, the angle $\overline{\theta}_H$ of low Co concentrations samples is reduced by at least $5°$ with respect to $Co_{0.3}^{Hpa}$ and $Co_{0.6}^{Hpa}$. As discussed theoretically hereafter, the abrupt change of phase for $\overline{\theta}_H$ results from a temperature related variation of the magnetic anisotropies.

The degree of organization of magnetic nanoparticles can be influenced by the presence of a magnetic field during a layer deposition. This can lead to a change in the dipolar interactions between the particles within the resulting structure. The phase of the precession for the $x = 0.3$ samples exposed to different magnetic fields during the film formation are displayed in Figure 4b. The use of a static magnetic field parallel to the substrate plane (Hpa) during the sample deposition decreases $\overline{\theta}_H$ by about $5°$ compared to Hpp and H0 deposition configurations. This is due to a lower degree of organization of the nCs as shown by SEM (Figures S7 and S8) which reduces the dipolar interactions between the nCs leading to a weaker demagnetizing field.

As shown in Figure 4c, the π-phase shift occurs for two different angles $\overline{\theta}_H$ when varying E_{pump}. It is due to the different origins of the shape and magneto-crystalline anisotropies that show distinct temperature dependencies. The former has a quadratic variation with the magnitude of the magnetization, while the latter has been shown for cobalt ferrites nanoparticles to vary exponentially with the square of the temperature.[30,50]

The magnetization precession has been modeled using the Landau–Lifshitz–Gilbert (LLG) equation (eq 1) coupled to the three temperature model (TTM) accounting for the dynamics of the charges, spins, and lattice temperatures (T_e, T_s, T_l) as shown in eq 2

$$(1 + \alpha^2)\frac{d\mathbf{M}}{dt} = -\gamma_0 \cdot \mathbf{M} \times \mathbf{H}_{eff}(T_s) - \frac{\alpha\gamma_0}{M_S(T_S)}[\mathbf{M} \times (\mathbf{M} \times \mathbf{H}_{eff}(T_s))]$$

$$(1)$$

$$C_e(T_e)\frac{dT_e}{dt} = G_{es}(T_s(t) - T_e(t)) + G_{el}(T_l(t) - T_e(t)) + P_{las}(t) - \frac{T_e(t)}{\tau_{diff}}$$

$$C_s(T_s)\frac{dT_s}{dt} = G_{es}(T_e(t) - T_S(t)) + G_{sl}(T_l(t) - T_s(t)) - \frac{T_s(t)}{\tau_{diff}}$$

$$C_l(T_l)\frac{dT_l}{dt} = G_{er}(T_e(t) - T_l(t)) + G_{sl}(T_S(t) - T_l(t)) - \frac{T_l(t)}{\tau_{diff}}$$

$$(2)$$

where γ_0, α, and T_S are the gyromagnetic factor, the damping parameter, and the spin temperature, respectively. In the TTM, C_e, C_s, and C_l are the electronic, magnetic, and lattice contributions to the specific heat, G_{el}, G_{es}, and G_{sl} are the electron–lattice, electron–spin, and spin–lattice coupling constants and τ_{diff} stands for the heat diffusion to the environment. We consider an equivalent reference system as the experimental geometry with the sample being in the xOy plane (see Figure 1a) and the axes of the cubic anisotropy along the system referential. An external magnetic field can be rotated in the xOy plane. In eq 3, the free energy, E, includes three contributions: cubic magneto-crystalline energy, Zeeman
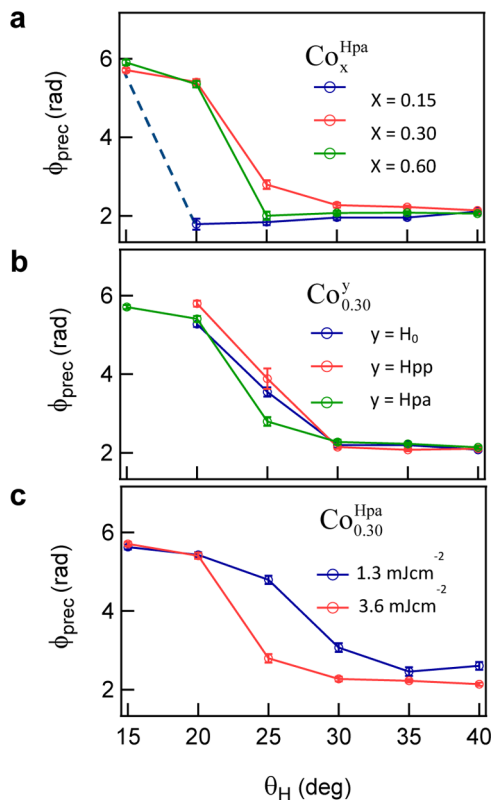

Figure 4. Precession characterization of $Co_xFe_{3-x}O_4$ nC single layers. Precession phase ϕ_{Prec} for (a) several cobalt concentrations x; (b) different magnetic fields y during the sample deposition; (c) two densities of the pump excitation E_{pump} for the sample $Co_{0.3}^{Hpa}$.

energy, and demagnetizing energy accounting for the shape anisotropy of the single layer nanoparticles.

$$E = [K_1(a_x^2 a_y^2 + a_x^2 a_z^2 + a_z^2 a_y^2) + K_2 a_x^2 a_y^2 a_z^2]$$
$$- \mu_0 M_s(a_x H_x + a_y H_y + a_z H_z) + \frac{1}{2}\mu_0 M_s^2 a_z^2 \qquad (3)$$

where K_1 and K_2 are the magneto-crystalline anisotropy constants, a_i are the cosine directions with $i = x, y, z$, μ_0 is the vacuum magnetic permeability, and H_i is the static applied magnetic field components in ith direction. The time dependent effective field, $\mathbf{H}_{eff} = \mathbf{H}_a + \mathbf{H}_Z + \mathbf{H}_d$, is obtained by the derivation of the free energy with respect to $\mathbf{M}$, where $\mathbf{H}_a$, $\mathbf{H}_Z$, and $\mathbf{H}_d$ are the magneto-crystalline anisotropy, Zeeman, and demagnetizing fields, respectively. The perturbation induced by the laser pulses is taken into account in the free energy via a modification of the anisotropy constant $K_1(T_s)$ as well as the amplitude of the saturation magnetization, $M_s(T_s)$, dependent on the temperature as

$$M_s(T_s(t)) = M_s(T_0)\sqrt{\frac{T_c - T_s(t)}{T_c}} \text{ for } T_s \le T_c$$

$$M_s = 0 \text{ for } T_s > T_c \qquad (4)$$

where T_c is the Curie temperature. The temperature variation of K_1 has been considered to be analogous to one measured for cobalt ferrite nanoparticles at high temperatures, that is, $K_1(T) = K_1(0)\exp(-\alpha T^2)$.

Figure 5 shows the effect of these parameters for a direct comparison with the experimental results (Figure 3). Figure 5a displays the simulated magnetization dynamics projected on the Oz axis (M_z) obtained for a system corresponding to the sample $Co_{0.3}^{Hpa}$. In the calculations, the room temperature SQUID measurements have been used to determine the M_s values. The interparticle dipolar interactions within the nC layer were introduced as an average demagnetizing field corresponding to the shape anisotropy of a continuous film with infinite lateral dimension, that is, $N_x = N_y = 0$; $N_z = 1$, where N_x, N_y, and N_z are the demagnetization factors. K_1 was the only adjustable parameter, selected such that $\overline{\theta_H}$ lies between 20° and 25°. Its value is close to the ones deduced from the SQUID measurements detailed in Section SI.III.3 of the Supporting Information.

The influence of the doping, the dipolar interactions (via N_z) and the pump intensity I_{pump} are presented in Figure 6 and correspond to the experimental results in Figure 4. Figure 6a displays the π-phase shift of the precession as observed experimentally in Figure 4a for $x = 0.3$ and 0.6. However, while the experimental transient measurements performed on samples with $x \le 0.15$ did not allow reliable ϕ_{Prec} values to be extracted, the modeling show that the angle $\overline{\theta_H}$ of low Co concentrations samples is reduced by 5° with respect to that obtained for $x = 0.3$. The K_1 value for $Co_{0.15}^{Hpa}$ was set to 73% of that used for $Co_{0.3}^{Hpa}$ and corresponds to the values extracted from SQUID measurements.

Figure 6b shows a variation of $\overline{\theta_H}$ of about 5° for $N_z = 1.0$ and 0.8, corresponding to the samples $Co_{0.3}^{Hpa}$ and $Co_{0.3}^{Hpp}$, respectively. The corresponding decrease of $\overline{\theta_H}$ is attributed to a reduction of the demagnetizing field with respect to the magneto-crystalline anisotropy. Two limit cases can be distinguished for the shape anisotropy, characterized by the ratio $N_x/N_z = N_y/N_z$, corresponding to two opposite interaction regimes. For $N_x = N_y = N_z = 1/3$ the nanocubes
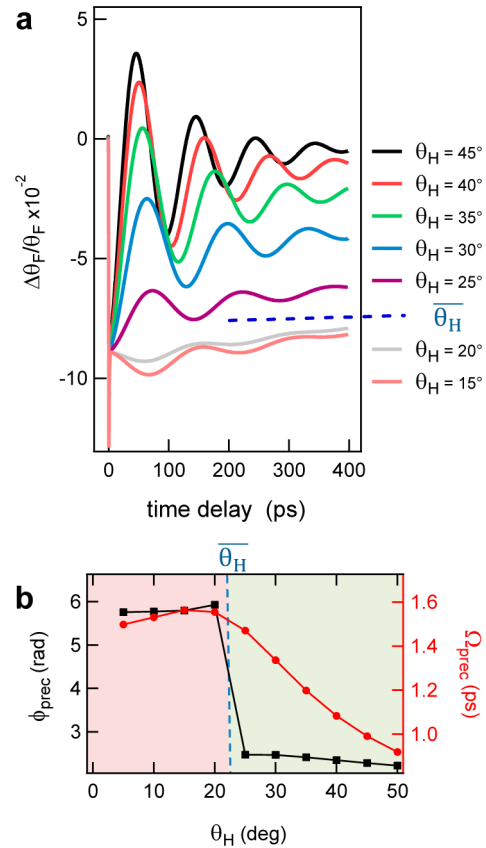

Figure 5. Modeling of the ultrafast magnetization dynamics of $Co_xFe_{3-x}O_4$ nC single layers. (a) Typical calculated time-resolved magneto-optical data obtained with the LLG equation coupled to the three temperature model. (b) Variation of the precession period (Ω_{Prec}, red circle) and phase (ϕ_{Prec}, black square) as a function of the magnetic field orientation (θ_H).

can be considered as isolated with their typical cubic symmetry, while $N_z = 1$, $N_x = N_y = 0$ corresponds to the bulk thin film limit. The intermediate situations correspond to an assembly of interacting particles that can be taken into account, for example, via different filling factors. In the following, we study the behavior of the π-phase shift associated with this intermediate regime of interaction. To investigate this issue it is important to consider the minimization of the free energy in the static case for various parameters, θ_H and E_{pump} or equivalently T_S, which is the equilibrium temperature between the charges, spins and lattice (considered as being achieved at time $t = 10$ ps in the following). Figure S14b shows the calculated change of magnetization orientation $[\theta_M(300\ K) - \theta_M(500\ K)]$ as a function of the external field direction θ_H. The set of curves correspond to different anisotropies from $N_z = 1$ (bulk thin film) to $N_z = 1/3$ (isolated nanocube) when the temperature increases from 300 to 500 K. For each curve, θ_M changes sign for a value $\overline{\theta_H}$ of θ_H that corresponds to the π-phase shift and that is plotted in Figure S14c. To evaluate which regime of interaction we have to consider for our nanocube layers, we made the same analysis for different temperatures. As shown in Figure S14d, the obtained set of curves (for $350 \le T_S \le 600$ K) allows a range of anisotropy ratios N_x/N_y to be defined to correspond to a range of critical angles $\overline{\theta_H}$ (see shaded area in Figure S14d), compatible with the experimental results of Figure 4c. For the observed angle $\overline{\theta_H} = 25°$ in Figure 4c, the
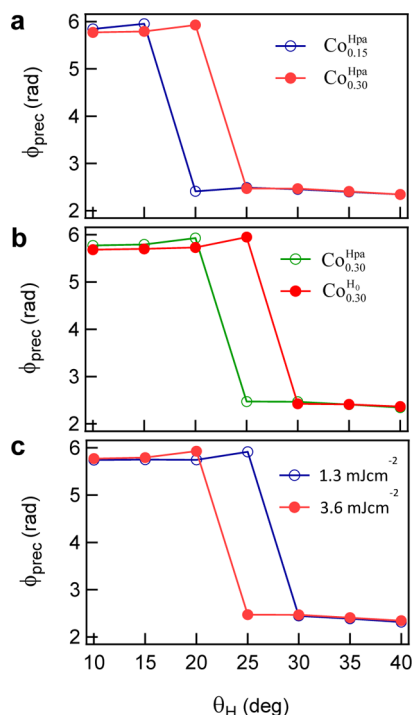
Figure 6. Precession modeling of Co$_x$Fe$_{3-x}$O$_4$ nC single layers. Precession phase (ϕ_{Prec}) for (a) two magneto-crystalline anisotropy constants; (b) degrees of the particles organization; (c) densities of the pump excitation E_{pump}.

anisotropy is different from the pure bulk thin film ($N_x = 0$, $N_z = 1$) and from the isolated cubes ($N_x = N_z = 1/3$). This study clearly establishes the effect of interparticle interactions via the shape anisotropy. At the end of Section SI−IV.1 in the Supporting Information, we show that the above considerations are valid for the temperatures of the sample derived either from the three temperature model and Curie−Weiss law or by the estimation of the temperature increase due to the sample absorption.

The experimental results of Figure 4c show that, when increasing E_{pump} by a factor 3, $\overline{\theta_H}$ decreases by 5°. This relatively large variation of $\overline{\theta_H}$ with E_{pump} can be advantageously used for controlling the phase of magnetic oscillators with laser intensity.

Let us now briefly consider the effect of disorder of the orientations of the nanocubes in the xOy plane (ϕ angle). In Section SI−IV.2 in the Supporting Information, an analysis has been performed over 138 nanocubes with a distribution of orientations corresponding to the disorder measured by SEM (Figure S7a1). Figure S15 shows that the corresponding distribution of angles $\overline{\theta_H}$ is very narrow. Indeed, the mean square value of 1.6° around $\overline{\theta_H} = 24°$ shows that the disorder does not essentially modify the π-phase shift behavior described above.

In conclusion, we have shown that a π-phase shift of the magnetization precession induced by femtosecond laser pulses in cobalt ferrite nanocubes occurs for particular angles of an applied external magnetic field. Its origin is demonstrated to be related to the competition between the temperature-dependent magneto-crystalline anisotropy of the nanocubes and the temperature-dependent demagnetizing field associated with the collective interactions between particles. These parameters

can be tuned with the doping of the nanocubes and the intralayer interactions, controlled at the time of the nanocube preparation and of their assembly, respectively. In addition, we have shown that the phase of the precession can be controlled by the intensity of the pump laser field. Our results bring valuable insights into the understanding of magnetization dynamics in confined magnetic nanosystems useful for applications in data storage and local magnetic sensing.

ASSOCIATED CONTENT

Supporting Information

The Supporting Information is available free of charge on the ACS Publications website at DOI: 10.1021/acs.nano-lett.6b02618.

Elaboration of Co$_x$Fe$_{3-x}$O$_4$ nCs, morphology and structural characterization, magnetic measurements, and characterization (PDF)

AUTHOR INFORMATION

Corresponding Authors
*E-mail: bigot@ipcms.unistra.fr.
*E-mail: vomir@ipcms.unistra.fr.
*E-mail: pjpandre@riken.jp.

Author Contributions

P.A., M.V., and J.Y.B. conceived the project. Under the supervision of P.A., I.B. developed the nanocubes synthesis and trained R.T., who then developed the organization of the nanocubes, synthesized, prepared, and characterized all the samples (XRD, SEM, SQUID). S.L.L. assisted the SQUID measurements. R.T. and P.A. analyzed complementary parts of the XRD and SQUID data. R.T. and M.V. optimized the sample preparation at IPCMS. M.V. and J.Y.B. performed the dynamic magnetization measurements; M.V. and J.Y.B. developed the modeling. P.P. and D.A.M. completed the measurements and analyses for both TEM and EELS. M.V., P.A., and J.Y.B. wrote the manuscript, which was revised by all coauthors.

ACKNOWLEDGMENTS

■ REFERENCES

(1) Mangin, S.; Ravelosona, D.; Katine, J. A.; Carey, M. J.; Terris, B. D.; Fullerton, E. E. *Nat. Mater.* **2006**, *5*, 210−215.

(2) Houssameddine, D.; Ebels, U.; Delaet, B.; Rodmacq, B.; Firastrau, I.; Ponthenier, F.; Brunet, M.; Thirion, C.; Michel, J. P.; Prejbeanu-Buda, L.; Cyrille, M. C.; Redon, O.; Dieny, B. *Nat. Mater.* **2007**, *6*, 447−453.

(3) Dobson, J. *Nat. Mater.* **2010**, *9*, 95−96.

(4) Kim, D.-H.; Rozhkova, E. A.; Ulasov, I. V.; Bader, S. D.; Rajh, T.; Lesniak, M. S.; Novosad, V. *Nat. Mater.* **2010**, *9*, 165−171.

(5) Nieves, P.; Chubykalo-Fesenko, O. *Phys. Rev. Appl.* **2016**, *5*, 2331−7019.

(6) Bigot, J.-Y.; Vomir, M. *Ann. Phys.* **2013**, *525*, 2−30.

(7) Beaurepaire, E.; Merle, J.; Daunois, A.; Bigot, J.-Y. *Phys. Rev. Lett.* **1996**, *76*, 4250−4253.

(8) Zhang, Q.; Nurmikko, A.; Anguelouch, A.; Xiao, G.; Gupta, A. *Phys. Rev. Lett.* **2002**, *89*, 177402−4.

(9) van Kampen, M.; Jozsa, C.; Kohlhepp, J.; LeClair, P.; Lagae, L.; de Jonge, W.; Koopmans, B. *Phys. Rev. Lett.* **2002**, *88*, 227201−4.

(10) Guidoni, L.; Beaurepaire, E.; Bigot, J.-Y. *Phys. Rev. Lett.* **2002**, *89*, 017401−4.

(11) Vomir, M.; Andrade, L.; Guidoni, L.; Beaurepaire, E.; Bigot, J.-Y. *Phys. Rev. Lett.* **2005**, *94*, 237601−4.

(12) Bigot, J.-Y.; Vomir, M.; Andrade, L. H. F.; Beaurepaire, E. *Chem. Phys.* **2005**, *318*, 137−146.

(13) Kimel, A. V.; Kirilyuk, A.; Usachev, P. A.; Pisarev, R. V.; Balbashov, A. M.; Rasing, T. *Nature* **2005**, *435*, 655−657.

(14) Malinowski, G.; Dalla Longa, F.; Rietjens, J. H. H.; Paluskar, P. V.; Huijink, R.; Swagten, H. J. M.; Koopmans, B. *Nat. Phys.* **2008**, *4*, 855−858.

(15) Bigot, J.-Y.; Vomir, M.; Beaurepaire, E. *Nat. Phys.* **2009**, *5*, 515−520.

(16) Radu, I.; Woltersdorf, G.; Kiessling, M.; Melnikov, A.; Bovensiepen, U.; Thiele, J. U.; Back, C. *Phys. Rev. Lett.* **2009**, *102*, 117201−4.

(17) Boeglin, C.; Beaurepaire, E.; Halte, V.; Lopez-Flores, V.; Stamm, C.; Pontius, N.; Durr, H. A.; Bigot, J.-Y. *Nature* **2010**, *465*, 458−462.

(18) Kim, J. W.; Vomir, M.; Bigot, J. Y. *Sci. Rep.* **2015**, *5*, 8511−7.

(19) Ikemiya, K.; Konishi, K.; Fujii, E.; Kogure, T.; Kuwata-Gonokami, M.; Hasegawa, T. *Opt. Mater. Express* **2014**, *4*, 1564−1573.

(20) Kovalenko, M. V.; Manna, L.; Cabot, A.; Hens, Z.; Talapin, D. V.; Kagan, C. R.; Klimov, V. I.; Rogach, A. L.; Reiss, P.; Milliron, D. J.; Guyot-Sionnnest, P.; Konstantatos, G.; Parak, W. J.; Hyeon, T.; Korgel, B. A.; Murray, C. B.; Heiss, W. *ACS Nano* **2015**, *9*, 1012−1057.

(21) Chen, S.; Hoskins, C.; Wang, L.; MacDonald, M. P.; André, P. *Chem. Commun.* **2012**, *48*, 2501−2503.

(22) Bigot, J. Y.; Kesserwan, H.; Halte, V.; Ersen, O.; Moldovan, M. S.; Kim, T. H.; Jang, J. T.; Cheon, J. *Nano Lett.* **2012**, *12*, 1189−1197.

(23) Chen, S.; Muldoon, M. J.; Anderson, K.; Andre, P. *CrystEngComm* **2011**, *13*, 3330−3333.

(24) Peddis, D.; Cannas, C.; Musinu, A.; Ardu, A.; Orrù, F.; Fiorani, D.; Laureti, S.; Rinaldi, D.; Muscas, G.; Concas, G.; Piccaluga, G. *Chem. Mater.* **2013**, *25*, 2005−2013.

(25) Hu, L.; de Montferrand, C.; Lalatonne, Y.; Motte, L.; Brioude, A. *J. Phys. Chem. C* **2012**, *116*, 4349−4355.

(26) Lee, N.; Choi, Y.; Lee, Y.; Park, M.; Moon, W. K.; Choi, S. H.; Hyeon, T. *Nano Lett.* **2012**, *12*, 3127−3131.

(27) Disch, S.; Wetterskog, E.; Hermann, R. P.; Salazar-Alvarez, G.; Busch, P.; Bruckel, T.; Bergstrom, L.; Kamali, S. *Nano Lett.* **2011**, *11*, 1651−1656.

(28) Li, L.; Yang, Y.; Ding, J.; Xue, J. M. *Chem. Mater.* **2010**, *22*, 3183−3191.

(29) Naik, S. R.; Salker, A. V. *J. Mater. Chem.* **2012**, *22*, 2740−2750.

(30) Franco, A.; Zapf, V. *J. Magn. Magn. Mater.* **2008**, *320*, 709−713.

(31) Nakagomi, F.; da Silva, S. W.; Garg, V. K.; Oliveira, A. C.; Morais, P. C.; Franco, A.; Lima, E. C. D. *J. Appl. Phys.* **2007**, *101*, 09M514−3.

(32) Yang, H.; Ogawa, T.; Hasegawa, D.; Takahashi, M. *J. Appl. Phys.* **2008**, *103*, 07D526−3.

(33) Kim, D.; Lee, N.; Park, M.; Kim, B. H.; An, K.; Hyeon, T. *J. Am. Chem. Soc.* **2009**, *131*, 454−455.

(34) Guardia, P.; Perez-Juste, J.; Labarta, A.; Batlle, X.; Liz-Marzan, L. M. *Chem. Commun.* **2010**, *46*, 6108−6110.

(35) de Montferrand, C.; Hu, L.; Milosevic, I.; Russier, V.; Bonnin, D.; Motte, L.; Brioude, A.; Lalatonne, Y. *Acta Biomater.* **2013**, *9*, 6150−6157.

(36) Tracy, J. B.; Crawford, T. M. *MRS Bull.* **2013**, *38*, 915−920.

(37) Ahniyaz, A.; Sakamoto, Y.; Bergstrom, L. *Proc. Natl. Acad. Sci. U. S. A.* **2007**, *104*, 17570−17574.

(38) Wang, M.; He, L.; Yin, Y. *Mater. Today* **2013**, *16*, 110−116.

(39) de Montferrand, C.; Lalatonne, Y.; Bonnin, D.; Lievre, N.; Lecouvey, M.; Monod, P.; Russier, V.; Motte, L. *Small* **2012**, *8*, 1945−1956.

(40) Singh, G.; Chan, H.; Udayabhaskararao, T.; Gelman, E.; Peddis, D.; Baskin, A.; Leitus, G.; Kral, P.; Klajn, R. *Faraday Discuss.* **2015**, *181*, 403−421.

(41) Kechrakos, D.; Trohidou, K. N.; Vasilakaki, M. *J. Magn. Magn. Mater.* **2007**, *316*, E291−E294.

(42) Du, H. F.; Du, A. *Phys. Status Solidi B* **2007**, *244*, 1401−1408.

(43) Correia, M. J.; Figueiredo, W.; Schwarzacher, W. *Phys. Lett. A* **2014**, *378*, 3366−3371.

(44) Russier, V.; de-Montferrand, C.; Lalatonne, Y.; Motte, L. *J. Appl. Phys.* **2013**, *114*, 143904−11.

(45) Russier, V. *J. Appl. Phys.* **2009**, *105*, 073915−9.

(46) Chen, T.-Y.; Hsia, C.-H.; Chen, H.-Y.; Son, D. H. *J. Phys. Chem. C* **2010**, *114*, 9713−9719.

(47) Hsia, C.-H.; Chen, T.-Y.; Son, D. H. *Nano Lett.* **2008**, *8*, 571−576.

(48) Hsia, C.-H.; Chen, T.-Y.; Son, D. H. *J. Am. Chem. Soc.* **2009**, *131*, 9146−9147.

(49) Maiti, S.; Chen, H. Y.; Chen, T. Y.; Hsia, C. H.; Son, D. H. *J. Phys. Chem. B* **2013**, *117*, 4399−4405.

(50) Franco, A.; e Silva, F. C. *Appl. Phys. Lett.* **2010**, *96*, 172505−3.